iet

Vibro-acoustic spectral analysis of low-field MRI

Swapnil Arawade, Janusz Piechowicz, and Tadeusz Pałasz

Abstract—Magnetic Resonance Imaging (MRI) is modern diagnostic tool to obtain internal images of human body. Vibration and noise are major challenges inherited by the MRI since their development. The paper analyses vibration and sound signals produced from the Low-field MRI system for different scanning sequences. Results from spectral analysis revealed strong relation between the vibration and sound signal, showing scanning sequence specific peaks at multiple frequencies. The results are useful to understand the dynamic nature of vibration and sound signal from MRI to develop the attenuation strategy.

Keywords—vibration; sound; Magnetic Resonance Imaging; Spectral analysis

I. Introduction

THE Magnetic Resonance (MR) Imaging (MRI) is important non-invasive diagnostic tool in modern medical practices. Enabling high-quality imaging of organs in human body without using ionizing radiation [1-3]. It has also importance in non-destructive testing of biomedical and agricultural samples [4-7]. The MRI scanners are generally classified according to their configuration, as closed and open type [8]. The working principle of all the MRI is moreover same. Generally, MR systems with static magnet strength lower than 1.5 Telsa are considered as low field MRI systems. The MRI systems having low field with open configuration have advantages of inexpensive production, compact installation, and lower risks [9,10]. Similar to the high magnetic field MRI, the low field MRI also leads to generation of vibration and noise during the operation. But, the noise is not much loud to produce risk for the patient but the induced vibration may result in reduced quality of the acquired images.

The MRI systems mainly consist set of gradient coils, Radio-Frequency (RF) coil and primary magnet to produces the stationary magnetic field. The gradient coils are responsible for spatial encoding of the MRI signal, while RF coils transmit and receive radio signals. During scan the set of electric pulses are given to the gradient coils, due to which gradient coils produce fast switching magnetic field around it. The magnetic field of gradient coils interferes with the magnetic field of primary magnet and leads to generation of Lorentz forces which sets the gradient coil in vibration. This vibration interacts with the surrounding media which is air and generates the typical sound of MRI scanner [11-15]. Also, these vibrations propagate to the scanning area and it can also induce secondary vibration of the

test object. These induced vibrations have reported to result in blurring effect in the MR images [16,17], especially in thin layer samples as well as sometime artifacts have been observed in the images [18].

Vibration of the gradient coil is the major challenge in low field as well as high field MRI systems. Scientific publication in the field have presented different approaches to improve the design of gradient coil and improvement methodologies majorly focused on hardware modifications and gradient pulse modifications [19-30]. Wang presented asymmetric gradient coil configuration to improve the performance with reducing the noise and vibration in the MRI system [31]. The spiral gradient coil with gradient derating presented by Zhou et. al. reported 16.6 dB(A) quieter operation, which indicates significant reduction in the vibration of gradient coil [32]. Boulent et al. investigated the path of vibration propagation in MRI scanner and proposed padding in the shield of RF coil to minimize the vibration and resulting noise during scans [33]. The pulse sequence modification is feasible method as compared to hardware modification. Wang et al. have designed polynomial function based gradient pulses which made the scans quieter by 18.6 dB(A) maintaining the similar signal to noise ratio and quality of image [34]. Wood et. al., presented modified MRI sequence based on zero echo time sequence, to replace the conventional most acoustically noisy fast gradient echo sequence and reported near silent scan with minimal extension of scan time [35]. Although, there has been significant progress in the field, the problem of vibration and noise remains present and better approach to resolve the problem is need.

The vibration and noise are the major challenges associated with low/high field open/closed configuration MRI systems. The main motive of this work is to investigate the detailed characteristics of vibration and resultant sound from the low field open MRI system during different scanning sequences. The input parameters of the electrical pulses provided to the gradient coil vary with different scanning sequences, leading to the expected changes in the properties of vibration and noise. In these systems the magnitude of vibration in the gradient coil is relatively smaller than high field MRI system and hence the noise generation mechanism can be investigated in deep. Also, the spectral characteristics reveal the dynamic properties of the signals. The results from the study will be useful in developing vibration mitigation strategy in low field MRI systems and proposing the noise reduction technique for high field MRI.

This work was supported by Faculty of Mechanical Engineering and Robotics, Department of Mechanics and Vibroacoustics, AGH University of Krakow, Poland from the finance source: 16.16.130.942/Piechowicz.

S. Arawade and J. Piechowicz are Faculty of Mechanical Engineering and Robotics, AGH University of Krakow, Poland. (e-mail: sarawade@agh.edu.pl,

ORCID: 0000-0003-1571-050X; piechowi@agh.edu.pl, ORCID: 0000-0002-1435-4673).

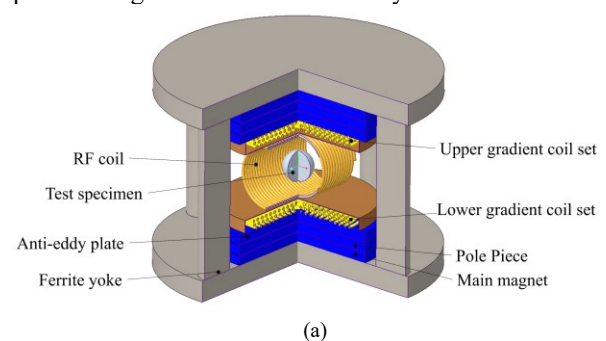
T. Pałasz is with Faculty of Physics, Astronomy and Applied Computer Science, Jagiellonian University in Kraków (email: tadeusz.palasz@uj.edu.pl , ORCID: 0000-0001-6707-4037).



II. MATERIALS AND METHODS

A. Data collection

The open configuration MRI scanner with low magnetic field generally has parallel arrangement of the gradient surface coils, located at top and lower part of the scanning area and the radio frequency coil is present between them in scanning zone. In this study, the vibration and sound measurements were performed for the weak magnetic field MRI scanner having static field strength (B0) of 89 mT and having scanning region of 10 cm (Make: MRI-Tech).[39] The vibrations of the gradient coil were measured using the digital accelerometer (model: Digiducer 333D01 USB accelerometer) placed directly on the plate of lower gradient coil. The accelerometer was connected to the computer through USB and further analyzed.



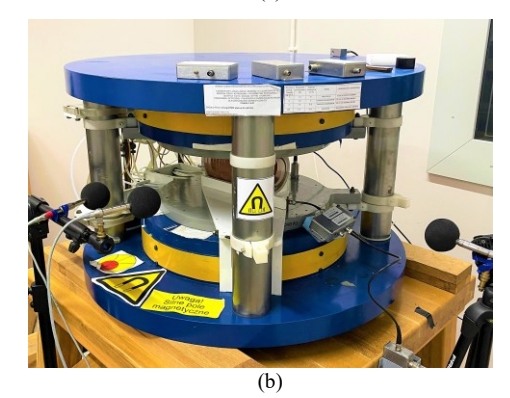


Fig. 1. Experimental setup a) Schematic of MRI system, b) actual MRI room setup

The sound signal was recorded using the free field omnidirectional microphone (SVANTEK 7052E) of ½ inch diameter with the frequency range of 20-20000 Hz. The microphone was positioned at 30 cm distance from the isocenter of the scanning area aligned with the axis of specimen. The microphone was connected to sound level meter (Make:

SVANTEK, model: SVAN971) by shielded cable. The doped water container was used as specimen for the imaging kept in the MRI scanning area. The construction and experimental setup is presented in the Fig. 1. The MRI control system was present in adjacent room and all the measurement equipment were operated from control room. The sampling frequency of the data collection devices was set to 12000 Hz and the setup was complaint to the NEMA MS-4 2023 standard for measurement of noise in MRI scanner. The investigation was carried out for the scanning sequences, namely: Fast Spin Echo (FSE), Spin Echo (SE) and Gradient Echo (GRE). The configuration parameters of these sequences are presented in the Table I.

B. Signal analysis

The data collected from the measurements from MRI scanner was processed and analyzed using the MATLAB ®2024a. In preprocessing, the signals were trimmed to eliminate the silent parts in the beginning and end of the sequence. The 15 seconds window from the signal was selected for analysis, to reduce the computation time. The trimmed vibration and sound signals were filtered using the bandpass filter, to focus majorly on the frequencies in the range of 100 Hz to 5000 Hz. The Fast Fourier Transform (FFT) analysis of the signal was performed to plot the frequency spectrum. The power spectral density (PSD) was determined to evaluate the distribution of power over the frequency. The expressions for vibration and sound signal PSD are shown in (1) and (2), respectively.

$$S_{xx}(f) = \frac{1}{N \cdot f_s} \cdot \left| X(f) \right|^2 \tag{1}$$

$$S_{yy}(f) = \frac{1}{N \cdot f_s} \cdot |Y(f)|^2 \tag{2}$$

where, $S_{xx}(f)$ is the PSD of vibration signal, $S_{yy}(f)$ is the PSD of sound signal, N is number of samples in time domain signal, f_s is the sampling frequency and X(f) and Y(f) are the Fourier transforms of discrete vibration and sound signals respectively. The obtained PSD was represented in the logarithmic scale of dB/Hz. The spectrogram of the signal was plotted to visualise the variation in the frequency characteristics over the time.

To understand the in-depth correlation between the vibration and sound signals, the Region of Interests (ROIs) were identified in the signals and selected for further analysis. Here, the ROIs were selected such that it consists single vibration pulse and corresponding sound signal. The signals trimmed in

TABLE I
SUMMARY OF THE SCANNING SEQUENCES USED IN 89 MILLITESLA MRI SCANNER

No.	Quantity	FSE	SE	GRE	Unit
1	Static field strength, (B0)	89	89	89	milliTesla (mT)
2	Repetition Time, (TR)	1000	1000	1000	milliseconds
3	Echo Time, (TE)	19	19	19	milliseconds
4	Number of slices	1	1	1	-
5	Slice thickness	200	200	200	millimeters (mm)
6	Field-of-view	200	200	200	millimeters (mm)
7	Scan Orientation)	Sagittal	Sagittal	Sagittal	-

Table shows the configuration of the 89mT open MRI scanner sequences

the ROIs were synchronized in order to eliminate the lag or error generated while trimming of ROI. The Cross Spectral Density (CSD) was determined for vibration and sound signal, which is the measure of similarity between the signals at each frequency. The expression of CSD is presented in (3) as follows:

$$S_{xy}(f) = \frac{1}{N \cdot f_s} \cdot X(f) \cdot Y^*(f) \tag{3}$$

where, $Y^*(f)$ represents the complex conjugate of Y(f). Further, time domain cross correlation analysis was performed on ROIs of the signals to compliment the CSD analysis. The Hilbert Transform was applied on the ROIs to obtain the amplitude modulation envelopes and normalized cross-correlation between envelopes using the expression (4):

$$R_{xy}(\tau) = \frac{\sum_{t} (|H\{x(t)\}| - \mu_{x}) (|H\{y(t+\tau)\}| - \mu_{y})}{\sqrt{\sum_{t} (|H\{x(t)\}| - \mu_{x})^{2} \sum_{t} (|H\{y(t+\tau)\}| - \mu_{y})^{2}}}$$
(4)

where, $|H\{x(t)\}|$ and $|H\{y(t)\}|$ represents the envelopes of vibration and sound ROIs calculated using Hilbert transform, μ_x and μ_y are the mean values of vibration and sound envelopes and τ represents the lag. The coupling strength (CS) was evaluated as the maximum value of $R_{xy}(\tau)$ in the range of $\pm \tau_{max}$.

The detailed frequency domain analysis was performed to investigate spectral characteristics of the signals such as determination of spectral centroid, bandwidth, flatness of the signal and spectral roll-off. The methodology for determining spectral characteristics of vibration signal is as follows:

The expression for spectral centroid C is shown in (5) as follows:

$$C = \sum_{i=1}^{N_f} f_i |X(f_i)|^2 / \sum_{i=0}^{N_f - 1} f_i |X(f_i)|^2$$
 (5)

where, f_i is the frequency at the ith bin, N_f is the total number of frequency bins and $|X(f_i)|^2$ is the power corresponding to frequency f_i .

Spectral bandwidth is the measure of spread of frequencies around the spectral centroid, and the expression for spectral bandwidth is presented in (6) as follows:

$$B = \sqrt{\sum_{i=1}^{N_f} (f_i - C)^2 \cdot |X(f_i)|^2 / \sum_{i=1}^{N_f} |X(f_i)|^2}$$
 (6)

Spectral flatness is the ratio of the geometric mean to the arithmetic mean of the power spectrum, the expression for spectral flatness is given in (7) as follows:

Flatness =
$$\sqrt[N_f]{\prod_{N_f}^{N_f} |X(f_i)|^2} / \frac{1}{N_f} \sum_{i=1}^{N_f} |X(f_i)|^2$$
 (7)

Spectral roll-off $f_{rolloff}$ is the frequency below which usually 85% of total power lies and is calculated from the relation presented in (8) as follows:

$$f_{rolloff} = \min \left\{ f_k \left| \sum_{i=1}^k |X(f_i)|^2 \ge \mathbf{\alpha} \cdot \sum_{i=1}^{N_f} |X(f_i)|^2 \right\}$$
(8)

where, α is the percentage of threshold power, f_k is the minimum frequency where cumulative power meets the threshold power.

Similarly, the spectral characteristics of sound signal were

calculated using Y(f). Further, the complete analysis was performed for all the vibration and sound signals recorded during three scanning sequences to determine the behaviour of system. The methodology in the form of flowchart is presented in Fig. 2.

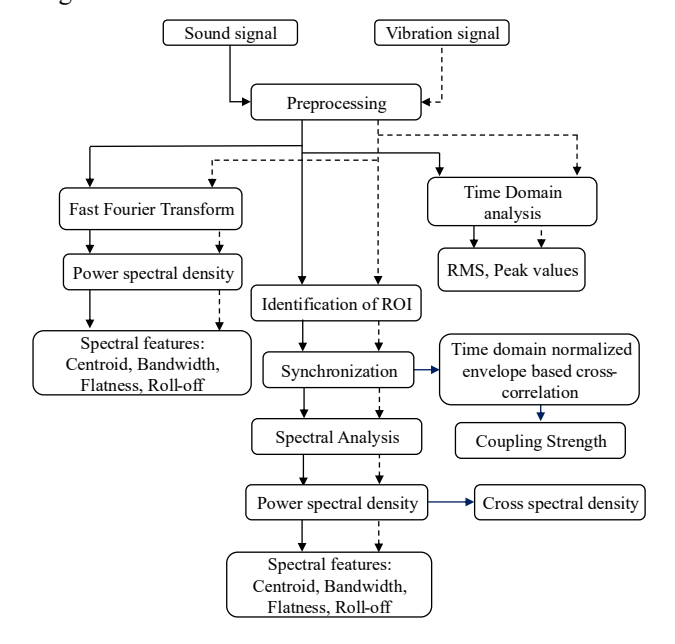


Fig. 2. Flow chart of the analysis

III. RESULTS

The vibration and sound signal generated by the low field MRI system were recorded during FSE, SE and GRE sequences. The NEMA MS-4 2023 suggests the typical response of MRI system lies within 5000 Hz, hence the sampling frequency for the data acquisition was set to 12000 Hz. The sound signal showed the background noise having frequency band of 0 to 100 Hz and hence during the analysis of the vibration and sound signal, the bandpass filter was used for the frequencies between $100\,\mathrm{Hz}$ to $5000\,\mathrm{Hz}$. Using the filtered vibration and sound signal waveforms, the spectrograms of the signals were evaluated to depict the dynamics of the signals over the duration of measurement. The single sided FFT spectrum referring to the Nyquist frequency was evaluated. Further, the PSD spectrum of the signals was determined for vibration and sound signals. The plots of the time domain waveform, spectrogram, FFT plot and PSD plot for vibration and sound signals recorded during FSE, SE and GRE scanning sequence are presented in the Fig. 3, 4 and 5, respectively.

The results from time domain analysis are presented in table II. spectrograms of the signals were evaluated to depict the dynamics of the signals over the duration of measurement. The spectral characteristics of the signals were evaluated and are presented in the Table III. The analysis revealed the distinct characteristics for the FSE, SE and GRE scanning sequence. The unique dominant frequencies were associated with each scanning sequence which was observed from the peaks in the vibration and sound signals visualised in the Fig. 4. It was figure revealed that majorly the dominant frequencies in vibration signal were in the range of 300 Hz to 1525 Hz. It is important to

notice that the spectral characteristics are being averaged out due to presence of silent parts as observed in vibration signals

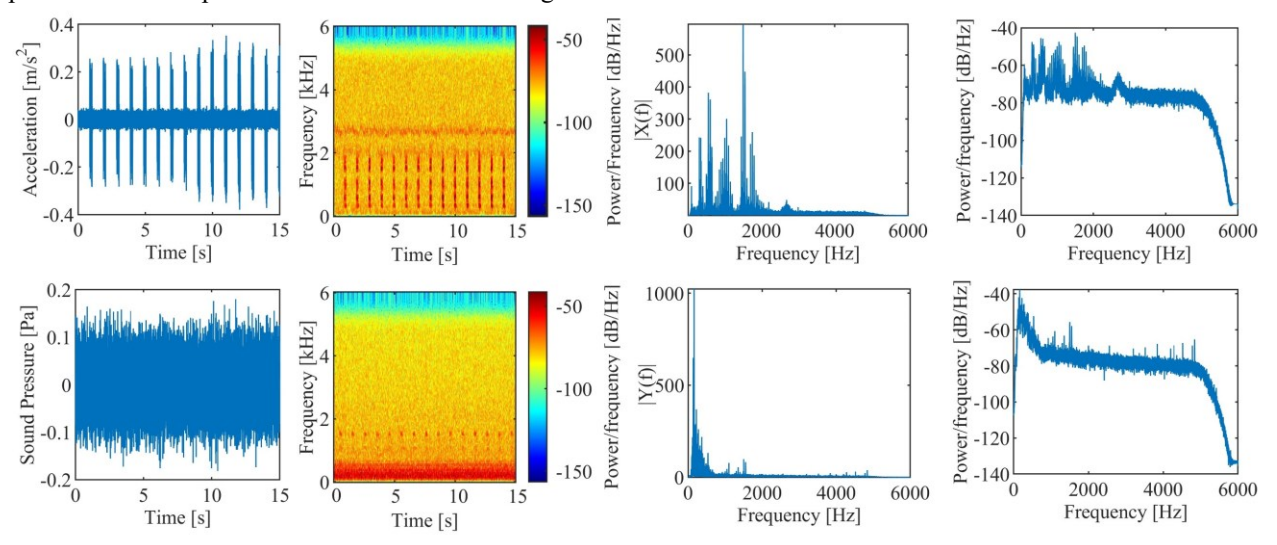


Fig. 3. Time-domain signal, spectrogram, FFT and PSD plot of vibration and sound signal for FSE scanning sequence

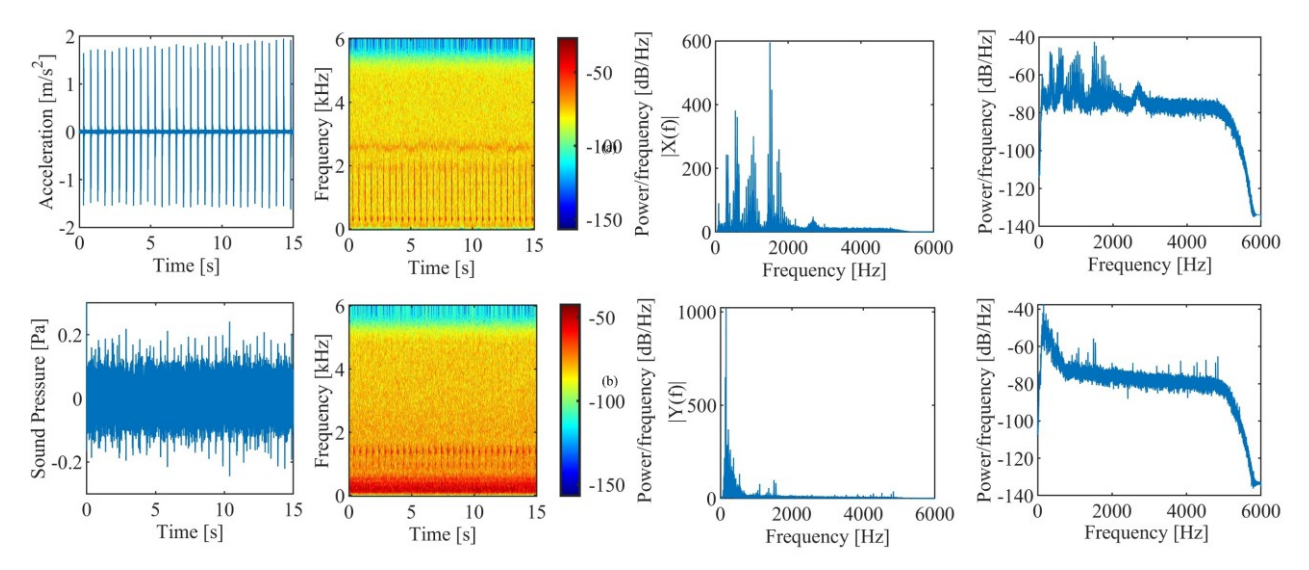


Fig. 4. Time-domain signal, spectrogram, FFT and PSD plot of vibration and sound signal for SE scanning sequence

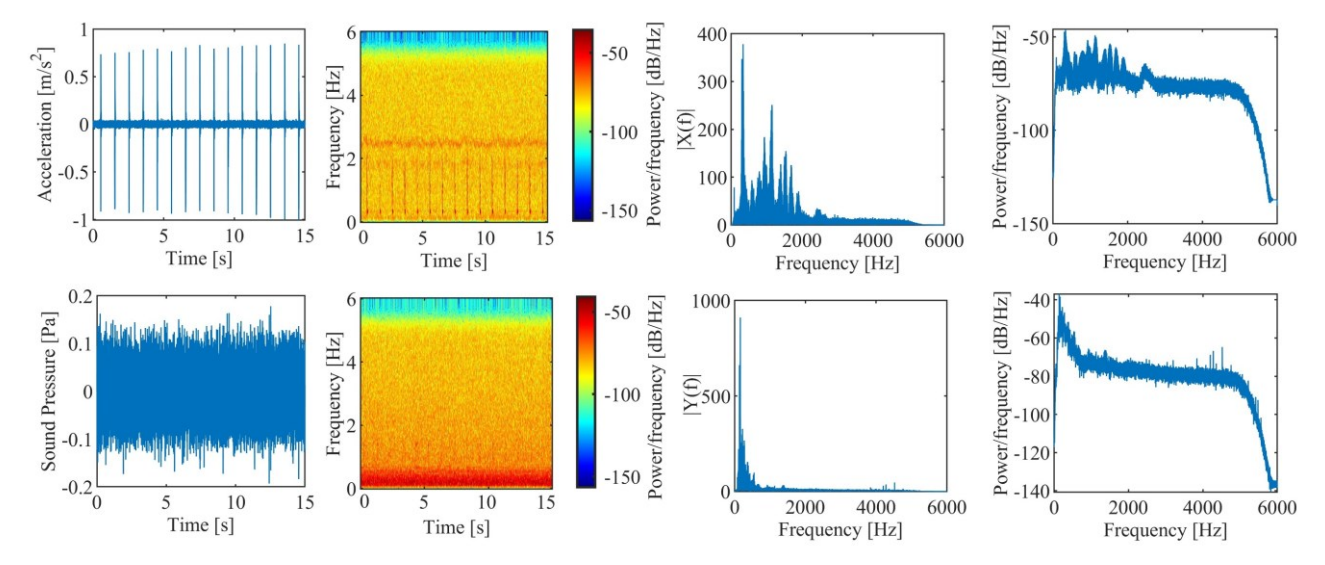


Fig. 5. Time-domain signal, spectrogram, FFT and PSD plot of vibration and sound signal for GRE scanning sequence

 $\label{total} TABLE~II$ TIME-DOMAIN ANALYSIS RESULTS OF SIGNALS FOR DIFFERENT SCANNING SEQUENCES

No.	Parameter	FSE	SE	GRE	Unit
1	Peak Sound Pressure	0.181407	0.356079	0.193119	Pascal (Pa)
2	Peak Acceleration	0.379766	1.948216	1.007687	(m/s^2)
3	RMS Sound Pressure	0.042826	0.043771	0.041386	Pascal (Pa)
4	RMS Acceleration	0.035385	0.112758	0.038354	(m/s^2)

TABLE III

SPECTRAL PROPERTIES OF COMPLETE SIGNALS FOR DIFFERENT SCANNING SEQUENCES

No.	Spectral Parameter	FSE	SE	GRE	Unit
1	Centroid (Sound pressure)	2079.2	1761.9	2029.9	Hz
2	Centroid (Acceleration)	1035.2	1119.5	1079.7	Hz
3	Bandwidth (Sound pressure)	1630.4	1334.8	1585.5	Hz
4	Bandwidth (Acceleration)	1560.1	1581.5	1575.7	Hz
5	Flatness (Sound pressure)	0.64	0.44	0.61	-
6	Flatness (Acceleration)	0.37	0.39	0.39	-
7	Roll-off (Sound pressure)	4203.3	3198.9	4102.6	Hz
8	Roll-off (Acceleration)	2829.9	2974.9	2929.2	Hz

To understand the correlation between the vibration and sound signal from low field MRI in more detail, the region of interest was selected consisting a single vibration pulse and corresponding sound signal for analysis. The frequency domain analysis method was adopted for investigation of signal characteristics and spectral properties. The synchronized signals and the results from frequency domain analysis such as magnitude spectrum and PSD of corresponding ROIs of vibration and sound signal for FSE, SE and GRE sequences are shown in the Figs. 6, 7 and 8 respectively. Cross spectral density analysis is the efficient way to investigate the correlation

between the power spectral densities of the two signals. The CSD of the vibration and sound signal was calculated as per the (3).

The results of the CSD evaluated for the different scanning sequences are presented in the Fig. 9. The figure shows significant correlation of the vibration and sound signal is bounded in the frequency range of 100 Hz to 2000 Hz. The CSD calculated for the FSE and SE scanning sequences shows the high correlation of the vibration and sound distributed around the frequency of 1500 Hz. The CSD of GRE scanning sequence shows high correlation of the frequencies lower than 1000 Hz.

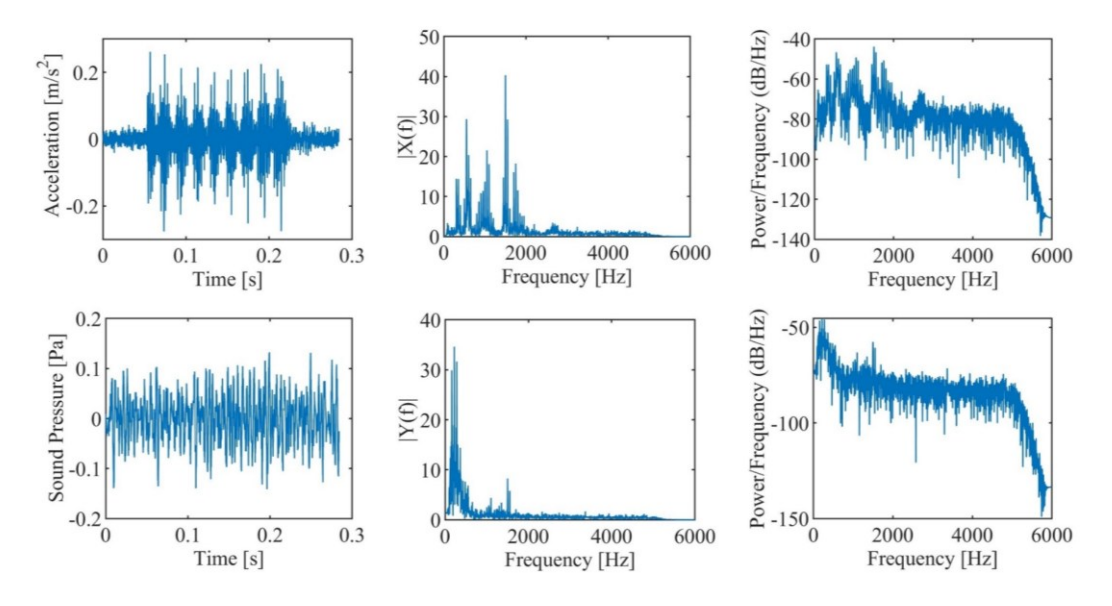


Fig. 6. Time-domain plot, FFT plot and PSD plot of synchronized ROI of vibration and sound signal for FSE scanning sequence

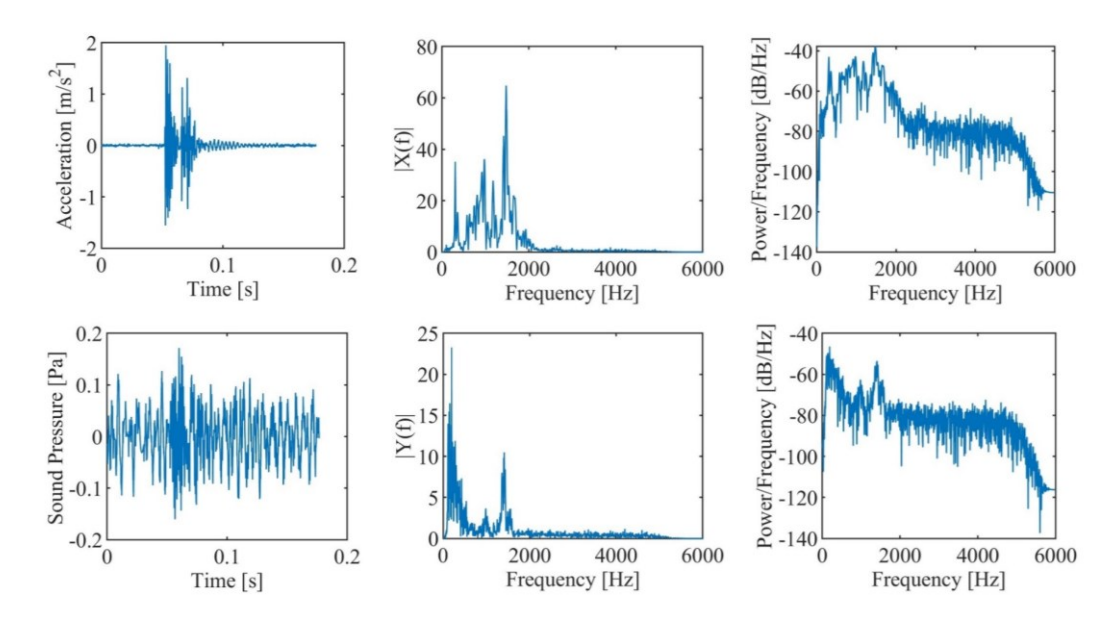


Fig. 7. Time-domain plot, FFT plot and PSD plot of synchronized ROI of vibration and sound signal for SE scanning sequence

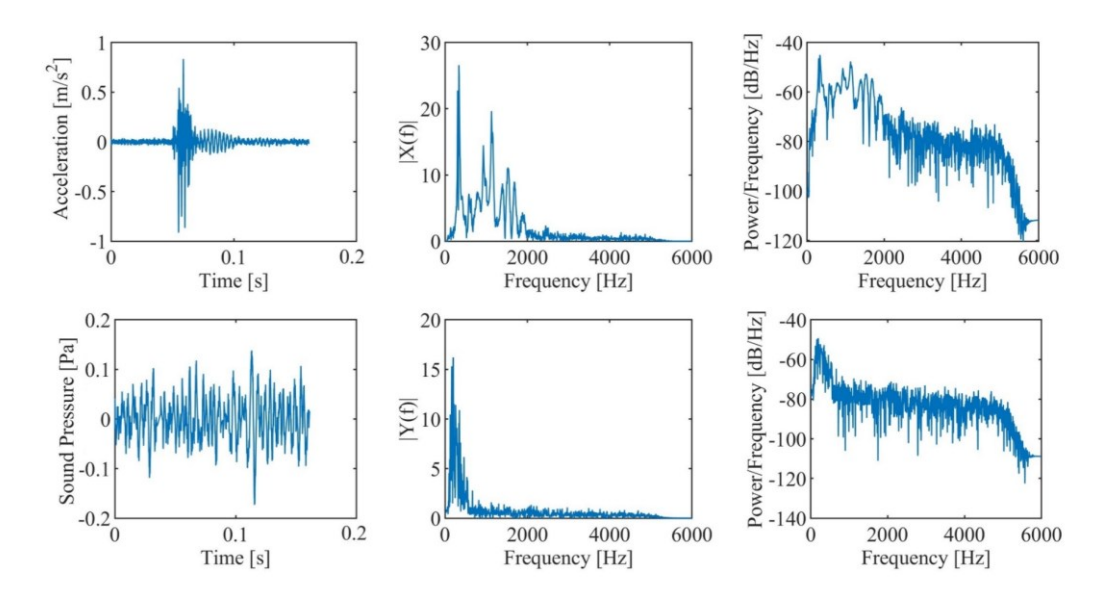


Fig. 8. Time-domain plot, FFT plot and PSD plot of synchronized ROI of vibration and sound signal for GRE scanning sequence

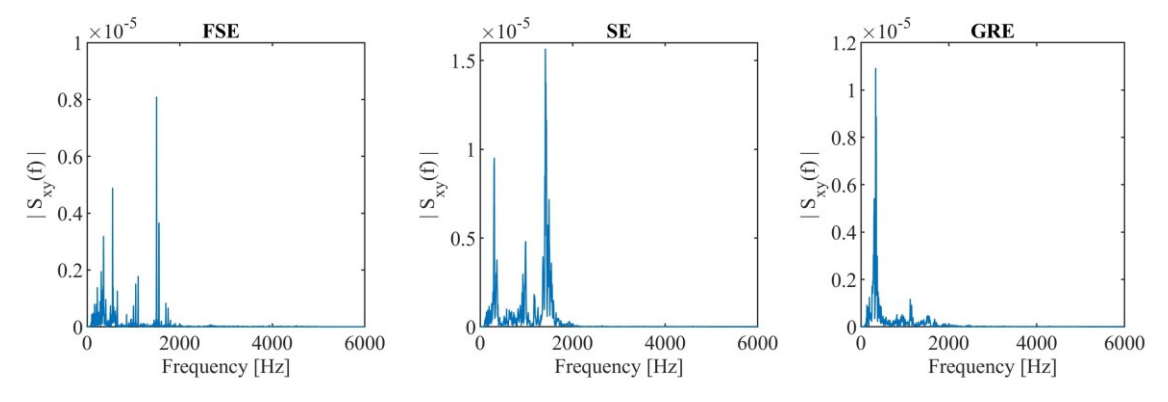


Fig. 9. Cross-spectral density plots of the vibration and sound signal synchronized ROIs identified during the scanning sequences of FSE, SE and GRE

No.	Spectral Parameter	FSE	SE	GRE	Unit
1	Centroid (Sound pressure)	1287.3	1285.7	1244.	Hz
2	Centroid (Acceleration)	1659.8	1310.2	1290.1	Hz
3	Bandwidth (Sound pressure)	1419.9	1287.8	1414.7	Hz
4	Bandwidth (Acceleration)	1290.3	723.0	944.1	Hz
5	Flatness (Sound pressure)	0.39	0.35	0.33	-
6	Flatness (Acceleration)	0.39	0.16	0.24	-
7	Roll-off (Sound pressure)	3112.9	2652.2	3080.3	Hz
8	Roll-off (Acceleration)	3024.8	1692.2	1874.2	Hz

 $\label{two} Table\ IV$ Spectral properties of trimmed-synchronized region of interests in signals

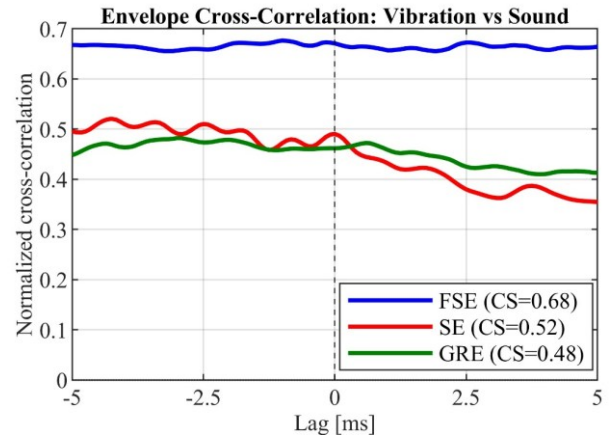


Fig. 10. Comparison of envelope cross correlation between vibration and sound signals recorded during different MRI scanning sequence.

Complementing to the CSD plots the envelope based cross correlation for the synchronized ROIs of vibration and sound signals during the different scanning sequences was evaluated and the coupling strength was calculated for the lag window of ± 5 ms as shown in Fig. 10. The vibration and sound signals in FSE scanning sequence showed highest cross correlation with maximum coupling strength of 0.68 while the signals during SE and GRE showed moderate similarity with coupling strength 0.52 and 0.48 respectively.

The spectral analysis of the ROIs of the vibration and sound signal of different scanning sequences are presented in the Table IV. The dominant frequencies in the signals are varying in between 300 Hz to 2000 Hz. The spectral analysis of the ROIs shorter duration leads to detection of transient events which may average out during the long signal analysis. The spectral centroid, bandwidth and roll-off provided the deep insights about the nature of the recorded signal. The spectral flatness of signal is evaluated for vibration and sound signal for different scanning sequences, and it is observed to be varying according to the scanning sequence. The vibration signal showed maximum spectral flatness for FSE sequence while sound signal showed for GRE sequence.

IV. DISCUSSION

The detailed analysis of the vibration and sound signals from the MRI for three different scanning sequences (FSE, SE, GRE) offers deep insights about characteristics, correlation, and spectral properties. The findings showed high implications for development of vibration control and noise reduction strategy. In case of low field open configuration MRI systems, the vibrations reaching to the scanning area is problematic as image quality is hugely impacted by movement of sample and can generate false results [16-17]. Thus, it is important to control the vibrations in the low field open configuration MRI systems. The sound generated during scanning in high field MRI have reported to reach up to 130 dB and is a major problem concerning the patient safety [36-38].

The maximum vibration magnitude was associated with SE scanning sequence for same configuration of the scanning sequences, as observed from the RMS values of the signals. The FFT spectrum and the PSD distribution depicted the dominance of the frequencies lower than 2000 Hz. The vibration signals shows association of multiple frequencies with higher power spectral densities showing broader band of dominant frequencies, while the sound signal FFT and PSD revealed the higher amplitude associated with the frequencies lower than the 1000 Hz. Distinct dominant frequency bands were identified for individual scanning sequence from the spectrograms of the recorded signals, highlighting dependency of vibration and noise signal characteristics on the type of scanning sequence. The vibration signals for all sequences have shown very high spectral flatness and higher value reaching up to 0.64 indicating highly noisy signal. But time domain signal shows idle period of 1 second between each vibration pulse, which is connected to repetition time in the scanning sequence configuration. Thus, the spectral properties when analysing the complete signal are averaged out. Hence, importance to study region of interests with shorter time, in this case a single vibration pulse and corresponding sound signal is justified.

The time domain plots of trimmed vibration and sound signal in the ROIs showed interesting characteristics which were missed out or averaged when complete signal under analysis. The vibration pulse in each of the scanning sequence significantly differ from each other. The time-domain plot shown in Fig. 6 of ROI in the FSE signal highlights a complex pulse with nine sub pulses with lower acceleration magnitudes. The corresponding ROI of sound signal is noisier showing influence of background noise on the recorded signal. The ROIs of SE sequence from Fig. 7 depicts a single pulse is composed of two high magnitude pulses resembling to the impulse response, where the magnitude was transiently diminishing. The

influence of the vibration pulse is clearly visible in the corresponding sound signal ROI, due to high magnitude of acceleration associated with the vibration pulse. The vibration signal ROI for scanning sequence of GRE represented in the Fig. 8 represents the typical signal reflecting characteristics of the impulse response. For GRE sequence, effect of vibration is not clearly visible in the corresponding sound signal.

The comparison of the ROIs of vibration and sound signal was carried out by the cross spectral density for FSE, SE and GRE scanning sequences. The comparison is depicted in the Fig. 9 reveals the significant relationship between the vibration and sound signal in the frequency band of 100-2000 Hz. In the CSD for FSE and SE scanning sequence at 1450 Hz the peak is observed and in case of GRE sequence the peak is associated with the frequency of 330 Hz. The peaks observed in the frequencies lower than 1000 Hz are consistent in all the sequences indicating the natural frequency of the system. Also, the time domain cross correlation revealed high coupling strength ranging from 0.48-0.68 for the vibration and sound signals depending upon the type of the scanning sequence. This confirms the transfer of energy from vibration to sound as observed in the CSD plots.

Considering the spectral properties of the ROIs presented in Table IV, the spectral centroid of the signals for scanning sequence FSE, SE and GRE indicated centroids of sound signal are lower than the corresponding vibration signal as well the bandwidth of sound signal is wider than the vibration signal, this can be explained by presence of low frequency background noise in the scanning room originating from the air handling system and radio frequency amplifier. The spectral flatness of the signals were identified in between the 0.16 to 0.39 in vibration and 0.33 to 0.39 in sound signals. The spectral flatness is the measure to quantify the noisiness of the power spectrum, here in case of vibration signal for SE sequence lower spectral flatness indicates few dominant frequencies and suggests more structuredness. Other signals with high values of spectral flatness shows that the signal is neither purely tonal nor completely noisy, i.e. it is combination of tonal and noise components and has more complex spectral content. These findings are important for understanding the characteristics of the vibration and sound signal in magnetic resonance imaging.

V. CONCLUSION

The study involved the investigation of characteristics of vibration and sound signal generated in the low field open configuration MRI scanner for different scanning sequences such as FSE, SE and GRE, at constant imaging parameters. The main aim of the study was to reveal the correlation between the vibration and sound in these MRI systems. Study presented the time-domain and frequencydomain analysis of the signals. The power spectra of the vibration and sound signals were compared utilizing the cross spectral density technique to locate the contribution of vibration in the generation of sound. In this analysis the presence of background noise in the frequency range of 0-100 Hz due to continuous operation air handling systems and radio frequency amplifier of MRI which was overcome by using the bandpass filter in the preprocessing of the signals. The analysis of ROIs revealed the consistent spectral profiles of the signals and revealed the significant dominance of a particular frequency band ranging from 100-2000 Hz. The spectral analysis of the ROIs revealed the complex nature of signals indicating the combination of tonal and noise components. The SE sequence had highest magnitude of vibration which depicted the strong relation between the vibration and sound signal with the same scanning parameters as that of other sequences. The important peak in the CSD were reported at 1450 Hz for FSE and SE sequences and 330 Hz for GRE sequence. The vibrations generated from the gradient coil, reaching to the scanning area to create disturbance in the test specimen is an important problem to address to make the images more clear, accurate and free from unknown artifacts. Similarly, high sound in high field MRI is a major concern for patient safety. The results from the study are particularly valuable for designing vibration and noise reduction strategy and improving the scan quality. The future work should explore the advanced materials and methods to further optimize the vibration and sound attenuation in MRI system, ensuring both operational efficiency and patient health.

REFERENCES

- [1] F. Bruno, F. Arrigoni, S. Mariani, A. Splendiani, E. Di Cesare, C. Masciocchi, A. Barile, "Advanced magnetic resonance imaging (MRI) of soft tissue tumors: techniques and applications," La radiologia medica, 124, pp. 243-52, 2019. https://doi.org/10.1007/s11547-019-01035-7
- [2] R. Reda, A. Zanza, A. Mazzoni, A. Cicconetti, L. Testarelli, D. Di Nardo, "An update of the possible applications of magnetic resonance imaging (MRI) in dentistry: a literature review," Journal of imaging, vol. 7(5), pp. 75, 2021. https://doi.org/10.3390/jimaging7050075
- [3] L. Landini, L.T. Mainardi, V. Positano, A.A. Young, M. Santarelli, L. Ying, W.E. Kyriakos, A.J. den Dekker, M. Styner, Y.O. Halchenko, A. Frangi, "Advanced image processing in magnetic resonance imaging," CRC press, Boca Raton, 2018. https://doi.org/10.1201/9781420028669
- [4] Y. Chen, "MRI Applications and Research in Materials Science," Science and Technology of Engineering, Chemistry and Environmental Protection, vol. 1(5), 2024. https://doi.org/10.61173/9d34fb93
- [5] T. Kim, J. Lee, G.M. Sun, B.G. Park, H.J. Park, D.S. Choi, S.J. Ye, "Comparison of X-ray computed tomography and magnetic resonance imaging to detect pest-infested fruits: A pilot study," Nuclear Engineering and Technology, vol. 54, no. 2, pp. 514-522, 2022. https://doi.org/10.1016/j.net.2021.07.015
- [6] S. Baek, J. Lim, J.G. Lee, M.J. McCarthy, S.M. Kim, "Investigation of the maturity changes of cherry tomato using magnetic resonance imaging," Applied Sciences, vol. 10, no. 15, pp. 5188, 2020. https://doi.org/10.3390/app10155188
- [7] C.L. Alves, J.S. Oliveira, A. Tannus, A.C.S.P. Tarpani, J.R. Tarpani, "Detection and imaging of damages and defects in fibre-reinforced composites by magnetic resonance technique," Materials, vol. 14, no. 4, pp. 977, 2021. https://doi.org/10.3390/ma14040977
- [8] E. Behluli, H.M. Preuer, N. Schiefermeier-Mach, R. Hornung, M. Küchler, M. Prokopetz, "Patient-centric comparative analysis of experiences in open upright and conventional closed MRI scanners," Radiography, vol. 30, no. 5, pp. 1258-1264, 2024. https://doi.org/10.1016/j.radi.2024.06.021
- [9] T.C. Arnold, C.W. Freeman, B. Litt, J.M. Stein, "Low-field MRI: clinical promise and challenges," Journal of Magnetic Resonance Imaging, vol. 57, no. 1, pp. 25-44, 2023. https://doi.org/10.1002/jmri.28408
- [10] J.P. Marques, F.F. Simonis, A.G. Webb, "Low-field MRI: An MR physics perspective," Journal of magnetic resonance imaging, vol. 49, no. 6, pp. 1528-1542, 2019. https://doi.org/10.1002/jmri.26637
- [11] Y. Zhang, X. Kong, W. He, Z. Xu, "Eddy Current Characterization Using Efficient Finite Element Analysis for Z-Gradient Coils in a Low-field MRI Scanner," IEEE Transactions on Instrumentation and Measurement, vol. 74, pp. 1-9, 2025. https://doi.org/10.1109/TIM.2025.3544743
- [12] P. Leo, A. D'Orazio, "Lorentz force and vibrations in transverse gradient coils in MRI." International Journal of Mechanical Sciences, vol. 288, p. 110011, 2025. https://doi.org/10.1016/j.ijmecsci.2025.110011

- [13] R.A. Hedeen, W.A. Edelstein, "Characterization and prediction of gradient acoustic noise in MR imagers," Magn Reson Med, vol. 37, pp. 7– 10, 1997. https://doi.org/10.1002/mrm.1910370103
- [14] P. Mansfield, P.M. Glover, J. Beaumont, "Sound generation in gradient coil structures for MRI," Magn Reson Med, vol. 39, issue 4, pp. 539–550, 1998. https://doi.org/10.1002/mrm.1910390406
- [15] A. Moelker, P.A. Wielopolski, M.T. Pattynama, "Relationship Between Magnetic Field Strength and Magnetic-Resonance-Related Acoustic Noise Levels," Mag. Reson. Mater. Phys., Biol. Med., 16(1), pp. 52–55, 2003. https://doi.org/10.1007/s10334-003-0005-9
- [16] D. Gallichan, J. Scholz, A. Bartsch, T.E. Behrens, M.D. Robson, K.L. Miller, "Addressing a systematic vibration artifact in diffusion-weighted MRI," Human brain mapping, vol. 31, no. 2, pp. 193-202, 2010. https://doi.org/10.1002/hbm.20856
- [17] E. Fuhrer, M. Jouda, C.O. Klein, M. Wilhelm, J.G. Korvink, "Gradient-induced mechanical vibration of neural interfaces during MRI," IEEE Transactions on Biomedical Engineering, vol. 67, no. 3, pp. 915-923, 2019. https://doi.org/10.1109/TBME.2019.2923693
- [18] I. Frollo, P. Andris, J. Pribil, V.Juras, "Indirect susceptibility mapping of thin-layer samples using nuclear magnetic resonance imaging," IEEE transactions on magnetics, vol. 43, no. 8, pp. 3363-3367, 2007. https://doi.org/10.1109/TMAG.2007.900571
- [19] Y. Hu, Q. Wang, X. Hu, X. Zhu, S. Crozier, Y. Wang, F. Liu, "A simulation study on the design of gradient coils in MRI for the imaging area above the patient bed," Measurement Science and Technology, vol. 28, no. 3, p. 035402, 2017. https://doi.org/10.1088/1361-6501/aa56cd
- [20] F. Jia, S. Littin, P. Amrein, H. Yu, A.W. Magill, T.A. Kuder, S. Bickelhaupt, F. Laun, M.E. Ladd M. Zaitsev, "Design of a high-performance non-linear gradient coil for diffusion weighted MRI of the breast," Journal of Magnetic Resonance, vol. 331, p. 107052, 2021. https://doi.org/10.1016/j.jmr.2021.107052
- [21] L. Xuan, X. Kong, J. Wu, Y. He, Z. Xu, "A smoothly-connected crescent transverse gradient coil design for 50mT MRI system," Applied Magnetic Resonance, vol. 52, no. 6, pp. 649-660, 2021. https://doi.org/10.1007/s00723-021-01330-5
- [22] S. Shen, N. Koonjoo, X. Kong, M.S. Rosen, Z. Xu, "Gradient coil design and optimization for an ultra-low-field MRI system," Applied Magnetic Resonance, vol. 53, no. 6, pp. 895-914, 2022. https://doi.org/10.1007/s00723-022-01470-2
- [23] B. De Vos, P. Fuchs, T. O'Reilly, A. Webb, R. Remis, "Gradient coil design and realization for a Halbach-based MRI system," IEEE Transactions on Magnetics, vol. 56, no. 3, pp. 1-8, 2022. https://doi.org/10.1109/TMAG.2019.2958561
- [24] X. Kong, Z. Xu, S. Shen, J. Wu, Y. He, L. Xuan, H. Igarashi, "Gradient coil design method specifically for permanent-magnet-type low field portable MRI brain scanner," IEEE transactions on instrumentation and measurement, vol. 72, pp. 1-12, 2022. https://doi.org/10.1109/TIM.2022.3225042
- [25] S. Nimbalkar, E. Fuhrer, P. Silva, T. Nguyen, M. Sereno, S. Kassegne, J. Korvink, "Glassy carbon microelectrodes minimize induced voltages, mechanical vibrations, and artifacts in magnetic resonance imaging,"

- Microsystems & nanoengineering, vol. 5, no. 1, p. 61, 2019. https://doi.org/10.1038/s41378-019-0106-x
- [26] C. Niu, H. Qu, "Numerical design of transverse gradient coil with transformed magnetic gradient field over an effective imaging area;" Magnetic Resonance Letters, p. 200139, 2024, https://doi.org/10.1016/j.mrl.2024.200139
- [27] J. Rösch, A. Mennecke, M. Knott, A. Doerfler, D.M. Grodzki, "Quiet FLAIR at 7T MRI," Investigative Radiology, vol. 55, no. 11, pp. 722-726, 2020. https://doi.org/10.1097/rli.000000000000094
- [28] X. Liu, "Development of Silent Multi-contrast Magnetic Resonance Imaging Acquisition Techniques," Doctoral dissertation, Technische Universität München, 2021. https://nbn-resolving.org/urn:nbn:de:bvb:91diss-20211216-1610202-1-4
- [29] D. Grodzki, F. Wiesinger, "Zero Acoustic Noise with Zero TE MRI, In MRI of Short-and Ultrashort-T2 Tissues: Making the Invisible Visible," Cham: Springer International Publishing, pp. 575-586, 2024. https://doi.org/10.1007/978-3-031-35197-6_46
- [30] S. Skare, T. Sprenger, O. Norbeck, H. Rydén, L. Blomberg, E. Avventi, M. Engström, "A 1-minute full brain MR exam using a multicontrast EPI sequence," Magnetic resonance in medicine, vol. 79, no. 6, pp. 3045-3054, 2018. https://doi.org/10.1002/mrm.26974
- [31] Y. Wang, "Gradient coil design and acoustic noise control in magnetic resonance imaging systems," Master's thesis, university of Queensland, Australia, 2014.
- [32] Z. Zhou, A. Alfayad, T.C. Chao, J.G. Pipe, "Acoustic noise reduction for spiral MRI by gradient derating," Magnetic Resonance in Medicine, vol. 90, no. 4, pp. 1547-1554, 2023. https://doi.org/10.1002/mrm.29747
- [33] N. Boulant, S. Ma, E. Walker, A. Beckett, A.T. Vu, S. Gunamony, D. A. Feinberg, "Acoustic noise reduction in the NexGen 7 T scanner," Magnetic Resonance in Medicine, 2024. https://doi.org/10.1002/mrm.30211
- [34] Y. Wang, P. Xu, J. Zeng, J. Zhang, Y. Zhu, S. Che, C. Yao, Y. Ge, C. Wang, "Sequence optimization for MRI acoustic noise reduction," Journal of Physics: Conference Series, Vol. 2591, No. 1, p. 012034, IOP Publishing, 2023. https://doi.org/10.1088/1742-6596/2591/1/012034
- [35] T.C. Wood, N.L. Damestani, A.J. Lawrence, E. Ljungberg, G.J. Barker, A.B. Solana, F. Wiesinger, S.C. Williams, "Silent myelin-weighted magnetic resonance imaging," Wellcome Open Research, vol. 5, 2020.
- [36] A. Moelker, P.M.T. Pattynama, "Acoustic noise concerns in functional magnetic resonance imaging," Hum Brain Mapp, vol. 20, pp. 123-141, 2003. https://doi.org/10.1002/hbm.10134
- [37] J. Hutter, A.N. Price, L. Cordero-Grande, "Quiet echo planar imaging for functional and diffusion MRI," Magn ResonMed, vol. 79, pp.1447-1459, 2018. https://doi.org/10.1002/mrm.26810
- [38] S. Arawade and J. Piechowicz. "Spectral Analysis of MRI Sound Signal." International Journal of Electronics and Telecommunications, vol. 70, no. 4, pp. 839-847, 2024. https://doi.org/10.24425/ijet.2024.152068
- [39] M. Suchanek, K. Cieślar, T. Pałasz, K. Suchanek, T. Dohnalik, Z.Olejniczak, "Magnetic Resonance Imaging at Low Magnetic Field Using Hyperpolarized ^3 He Gas", Acta Physica Polonica A, tom 107, nr 3, s. 491-506, 2005. https://www.doi.org/10.12693/APhysPolA.107.491